



Attosecond Plasma Wave Dynamics in Laser-Driven Cluster Nanoplasmas

Charles Varin,^{1,*} Christian Peltz,² Thomas Brabec,¹ and Thomas Fennel^{2,†}

¹*Department of Physics, University of Ottawa, 150 Louis Pasteur, Ontario K1N 6N5, Canada*

²*Institut für Physik, Universität Rostock, 18051 Rostock, Germany*

(Received 8 August 2011; published 24 April 2012)

We introduce a microscopic particle-in-cell approach that allows bridging the microscopic and macroscopic realms of laser-driven plasma physics. As a first application, resonantly driven cluster nanoplasmas are investigated. Our analysis reveals an attosecond plasma-wave dynamics in clusters with radii $R \approx 30$ nm. The plasma waves are excited by electrons recolliding with the cluster surface and travel toward the center, where they collide and break. In this process, energetic electron hot spots are generated along with highly localized attosecond electric field fluctuations, whose intensity exceeds the driving laser by more than 2 orders of magnitude. The ionization enhancement resulting from both effects generates a strongly nonuniform ion charge distribution. The observed nonlinear plasma-wave phenomena have a profound effect on the ionization dynamics of nanoparticles and offer a route to extreme nanoplasmonic field enhancements.

DOI: [10.1103/PhysRevLett.108.175007](https://doi.org/10.1103/PhysRevLett.108.175007)

PACS numbers: 52.38.-r, 52.65.-y, 71.45.Lr

A key challenge in modeling laser-driven plasmas is to properly resolve both microscopic and macroscopic phenomena. Microscopic processes, such as atomic collisions, require Angstrom resolution, while the macroscopic scale is determined by the laser wavelength. For example, an exact classical analysis of near-infrared laser-driven solid-density plasmas requires us to resolve 4 orders of magnitude in space (from \AA to μm) and to trace 10^{10} classical particles along with laser propagation. Currently, no numerical method can fulfill all these demands. The most common numerical tools are electrostatic molecular dynamics (MD) [1] and the particle-in-cell (PIC) method [2–4]. Both have their merits and limitations.

In the electrostatic limit, classical plasma dynamics is described exactly by MD. Newton's equations are solved for all charged particles and the sum over all binary Coulomb forces can be efficiently done by tree [5,6] or particle-particle-particle-mesh (P³M) methods [7]. MD works well for small nanoplasmas (clusters), where the dipole approximation and the neglect of field propagation are justified [8,9]. It has revealed the importance of microscopic processes, such as collisions and plasma microfields, in dense nonrelativistic plasmas [8,9].

Wave propagation phenomena, however, require the solution of Maxwell's equations and are studied by PIC codes [2–4]. Typically, Maxwell's equations are solved on a grid along with the relativistic equations of motion for all PIC particles [10–12]. As one PIC particle represents many microscopic particles, fine-grained atomic processes are lost. Collisions can be reintroduced via Monte Carlo methods [13,14]. This is valid for weak coupling, where microfield fluctuations are negligible and microscopic interactions are limited to small-angle binary collisions.

The nonrelativistic dynamics of laser-driven clusters and bulk materials proceeds far from equilibrium and is

strongly coupled [15,16]. In this realm, standard kinetic theory fails and collisional PIC misses important effects: (i) As the local temperature and the Coulomb logarithm cannot be defined unambiguously, scattering rates cannot be quantified; (ii) many-particle recombinations via three and more body collisions become important; (iii) plasma microfields enhance field and impact ionization [17,18]; (iv) PIC particles exceed the surface length scale, prohibiting a quantitative account of surface phenomena.

The microscopic particle-in-cell concept, MPIC, was developed to address the shortfalls of MD and PIC [19]. PIC particles and grid spacing (Δx) are shrunk to ≈ 1 \AA to represent single physical particles. The fields obtained from Maxwell's equations then contain all microscopic interactions. Therefore, the classical plasma dynamics is modeled exactly, as in MD, and wave propagation is accounted for as well. However, as the solution of Maxwell's equations scales with ($\propto 1/\Delta x^4$), modeling simulation volumes big enough to bridge microscopic and macroscopic realms has been out of reach so far.

In this Letter, we introduce a new microscopic particle-in-cell method named MicPIC that overcomes the above limitations of the MPIC scheme with a P³M force splitting. In MicPIC, long-range electromagnetic interactions are treated on a PIC level with particles represented by wide Gaussian profiles on a coarse grid. When two particles come close, the PIC field is replaced by the electrostatic one to resolve microscopic (Mic) interactions. MicPIC can currently track 10^7 particles on a single CPU (10^{10} expected with parallelization). The microscopic resolution with comparable particle numbers was so far restricted to electrostatic P³M [7] or tree schemes [5], which, however, neglect laser propagation and magnetic fields. MicPIC opens up new frontiers by enabling a classically

exact, microscopic analysis of macroscopic laser-matter processes.

As a first application, we study resonant Mie plasmon excitation of metal-like cluster nanoplasmas. A comparison with MD and Mie theory validates MicPIC and shows that propagation effects notably modify the absorption for cluster radii $R \gtrsim 20$ nm: i.e., an electrostatic treatment is no longer justified. Our main finding is the excitation of plasma waves in these surprisingly small clusters at moderate laser intensities ($< 10^{14}$ W/cm²). They are created by electrons recolliding with the cluster surface and propagate into the cluster. The spherical cluster geometry focuses the waves toward the cluster center, where they collide and break. This results in the enhanced generation of fast electrons near the cluster center and in strong attosecond electric field fluctuations. Both effects augment ionization and create a strongly nonuniform ion charge distribution.

In MicPIC, each actual plasma particle (electron or ion) is described by a charge density $\rho_i(\mathbf{r}) = q_i g(|\mathbf{r} - \mathbf{r}_i|, w_0)$, where q_i and \mathbf{r}_i are the charge and position of the i th particle and $g(r, w) = \exp(-r^2/w^2)/\pi^{3/2}w^3$. The finite effective width w_0 of the particle emulates its quantum nature and the resulting softening of Coulomb interactions. The propagation of the laser field and particles is done in a two stage process: (i) Long-range forces and radiation are described *via* the electromagnetic PIC method on a grid; (ii) short-range interactions are determined by a local (gridless) electrostatic MD on the microscopic (Mic) level. These two stages motivate the name MicPIC.

On the PIC level, particles are represented by a charge density $\rho_i^{\text{pic}}(\mathbf{r}) = q_i g(|\mathbf{r} - \mathbf{r}_i|, w_{\text{pic}})$ whose width is larger than the actual particle width ($w_{\text{pic}} \gg w_0$). As a result, interactions of nearby particles are underestimated. The necessary short-range correction contributes only for $r_{ij} = |\mathbf{r}_j - \mathbf{r}_i| < r_{\text{cut}}$ with cutoff radius $r_{\text{cut}} \approx 3w_{\text{pic}}$.

The total MicPIC force on the i th particle reads

$$\mathbf{f}_i = -\sum_j \nabla_{\mathbf{r}_i} V_{ij}^{\text{mic}} + \int \rho_i^{\text{pic}} [\mathbf{E}^{\text{pic}} + \dot{\mathbf{r}}_i \times \mathbf{B}^{\text{pic}}] d^3r, \quad (1)$$

where V_{ij}^{mic} represents the local correction potential (Mic). The second term includes the electromagnetic fields \mathbf{E}^{pic} and \mathbf{B}^{pic} sampled on the PIC grid. Fields and particles are propagated by solving self-consistently (i) the classical equations of motion for all particles subject to the force in Eq. (1) and (ii) Maxwell's equations using the PIC charge and current densities $\rho^{\text{pic}} = \sum_i \rho_i^{\text{pic}}$ and $\mathbf{j}^{\text{pic}} = \sum_i \dot{\mathbf{r}}_i \rho_i^{\text{pic}}$, respectively. For a detailed derivation see the Supplemental Material in [20].

Finally, it should be noted that MicPIC contains both PIC ($w_{\text{pic}} = w_0$) and MD ($w_{\text{pic}} \rightarrow \infty$) as limiting cases. Further, MicPIC scales linearly with particle number N and load balancing between Mic and PIC parts can be adjusted by varying w_{pic} ; see [20].

As a metal cluster model system, we study preionized spherical nanoplasmas in 800 nm laser pulses [Gaussian field envelope $\exp(-t^2/\tau^2)$, $\tau = 7$ fs, flat beam profile, polarized along x , propagation along z]. The MicPIC parameters are a 300^3 -cell PIC grid with mesh size $\Delta x = 5$ Å, uniaxial perfectly matched layer boundary conditions [21], a PIC particle width $w_{\text{pic}} = 1.15\Delta x$, and a cutoff $r_{\text{cut}} = 3\Delta x$ (see [20]).

We first study the role of propagation effects for the nearly linear excitation of resonant clusters at intensity 6×10^{11} W/cm². The cluster for MicPIC and MD analysis is modeled by one conduction electron per ion, fcc structure, and ionic Wigner-Seitz radius $r_s = 3.6$ Å (Mie plasmon at 800 nm); the ionization of bound atomic electrons is disregarded. Further, we use an initial electron temperature $T_e = 5$ eV and a particle width $w_0 = 1$ Å (electrons and ions). This system allows us to validate MicPIC by comparison to well-established theories; see Fig. 1.

In the small-cluster limit, propagation effects are negligible and MD describes the classical cluster dynamics exactly. As the excitation takes place in the linear response regime, MicPIC results for large clusters can be compared with Mie theory [22], which fully accounts for propagation effects. In the small-cluster electrostatic limit, Mie theory simplifies to the so-called nanoplasma model [23] (see [20] for further details). For both analytic models (Mie and nanoplasma), the laser pulse spectrum was taken into account. In both, Mie and nanoplasma theory, microscopic interactions are contained in a Drude dielectric function $\varepsilon(\omega) = 1 + \chi_0 - \omega_p^2/(\omega^2 + i\omega\nu)$, with χ_0 a real valued background susceptibility, ν the collision frequency, and $\omega_p = \sqrt{e^2 n_e / m_e \varepsilon_0}$, the plasma frequency. For a perfectly metallic sphere, the Mie plasmon frequency is $\omega_{\text{mie}} = \omega_p / \sqrt{3}$. The collision frequency is a function of the cluster radius $\nu(R) = \nu_0 + \nu_1/R$, containing volume and surface terms. Matching the nanoplasma model to MD results (see [20]) yields the coefficients $\chi_0 = 0.15$, $\nu_0 = 0.102$ fs⁻¹,

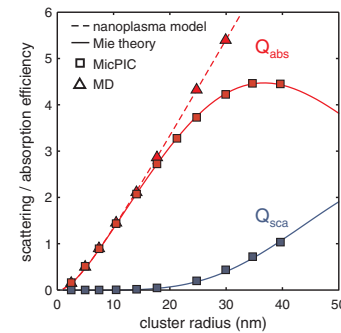


FIG. 1 (color). Absorption (Q_{abs}) and scattering (Q_{sca}) efficiency of preionized clusters excited at resonance (800 nm) by 7 fs laser pulses with peak intensity 6×10^{11} W/cm². The efficiencies reflect the absorbed or scattered energy normalized by the laser energy flow through the geometrical cluster cross section.

and $v_1 = 2.4 \text{ nm fs}^{-1}$, which are used in the Mie model to validate MicPIC.

The MicPIC and MD data in Fig. 1 agree well for small clusters, proving that MicPIC accounts correctly for collisions. Excellent agreement of MicPIC and Mie theories for all sizes proves the correct account of macroscopic optical effects. Reduced MicPIC absorption for $R \gtrsim 20 \text{ nm}$ (compared to MD) reflects radiation damping as a clear sign of propagation effects. Values of Q_{abs} beyond unity for $R \gtrsim 8 \text{ nm}$ imply absorption cross sections higher than the geometric cross sections (absorption paradox).

In the second part, nonlinear, resonant cluster excitation at higher intensity ($6 \times 10^{13} \text{ W/cm}^2$) is studied, which reveals new dynamical effects. The high cluster microfields and electron energies require a treatment of impact and tunnel ionization including their enhancement by plasma fields; our implementation follows Ref. [18].

In experiments, resonance is established by a cluster expansion after 0.1–1 ps. As MicPIC cannot cover such times without parallelization, we model only the second stage of a pump-probe scenario. In the first stage, a pump pulse is assumed to preionize a Xe cluster. Our MicPIC analysis starts when the expanding cluster is in resonance with the probe pulse (800 nm). As an initial condition, we assume a charge neutral, $R = 30 \text{ nm}$ cluster with a homogeneous ion charge state Xe^{4+} and ion Wigner-Seitz radius $r_s = 5.6 \text{ \AA}$; electrons are relaxed to a steady state with a temperature of 4 eV. Runs with smaller clusters corroborate our idealized initial condition. For moderate pump intensities ($\lesssim 10^{14} \text{ W/cm}^2$) and pulse durations ($\gtrsim 50 \text{ fs}$), cluster expansion and ion charge distribution are fairly uniform and electron loss is negligible. The

charge state and electron temperature are representative for the above pump laser parameters.

Snapshots of the cluster probe-pulse interaction are shown in Fig. 2; plots (a)–(f) show the total charge density at various times; in the inset the times are put in relation to the laser field and dipole moment. Plasma waves are produced at the cluster poles (intersection of the surface and x axis) and propagate into the cluster 2(a) and 2(b). With a rising dipole amplitude, plasma waves get stronger and penetrate deeper into the cluster [Fig. 2(c)]. They are a mixture of spherical and plane waves, as they evolve in the mixed geometry of a sphere and a linear cluster polarization field. When the waves reach the center and collide [Fig. 2(d)], wave breaking and turbulent electron dynamics are observed [Fig. 2(e) and 2(f)].

The electron phase-space distributions $f(x, v_x)$ in Figs. 2(g)–2(l) reveal the origin of the plasma-wave dynamics. Figure 2(g) shows a tail at the left side of the cluster that was driven out of the cluster in the previous half cycle, when the electron cloud was pushed over the left cluster boundary. At the time of the snapshot (g), the main cloud has moved to the right, leaving behind unscreened ions at the left border [yellow region in Fig. 2(a)]. The resulting polarization force accelerates part of the escaping electrons back into the cluster. When they hit the surface, a plasma wave is created [Fig. 2(h)] and propagates into the cluster together with the recollided electron bunch [Fig. 2(i)]. Near the pulse peak, these particle-wave bunches travel deeper and faster into the cluster. Wave breaking occurs when the plasma waves from the left and right surface reach the center and collide [Fig. 2(j)], leading to strong fragmentation of the

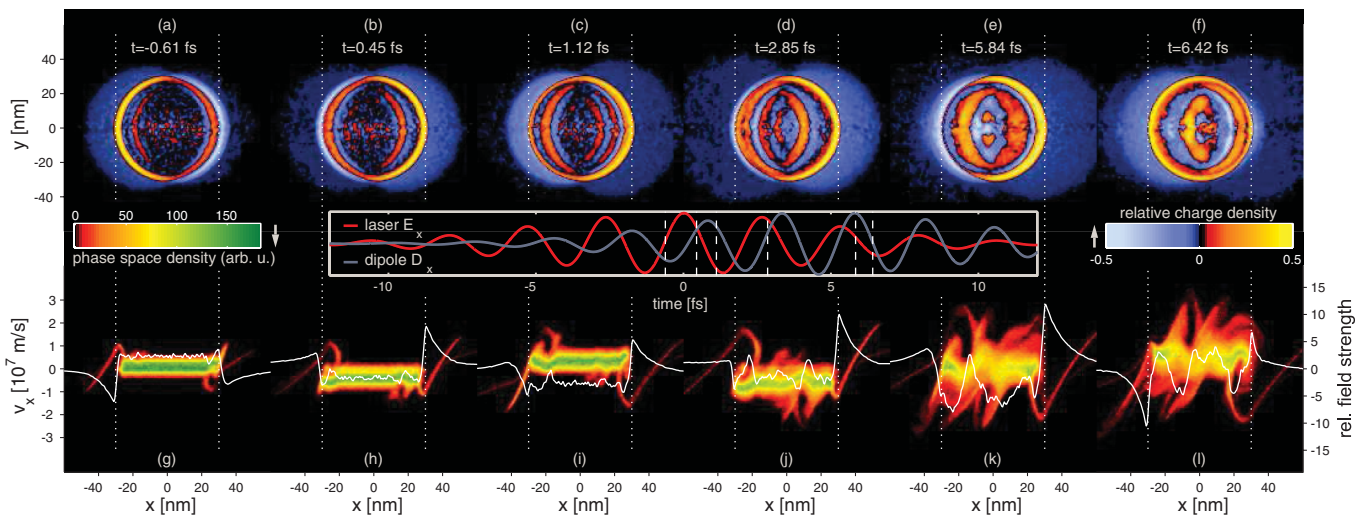


FIG. 2 (color). Time evolution of a $R = 30 \text{ nm}$ Xe^{4+} cluster excited at resonance (800 nm) by a 7 fs laser pulse with peak intensity $6 \times 10^{13} \text{ W/cm}^2$. The top panels (a)–(f) show the charge density (relative to the ion density) in the x - y plane at various times; times are also indicated as vertical lines in the plot of the laser field and dipole moment (see inset in the middle). The lower panels (g)–(l) show the corresponding electron density in phase space $f(x, v_x)$ evaluated on the x axis. The x component of the electric field (normalized to the peak laser field) is shown as a white curve on top of the phase-space graphs.

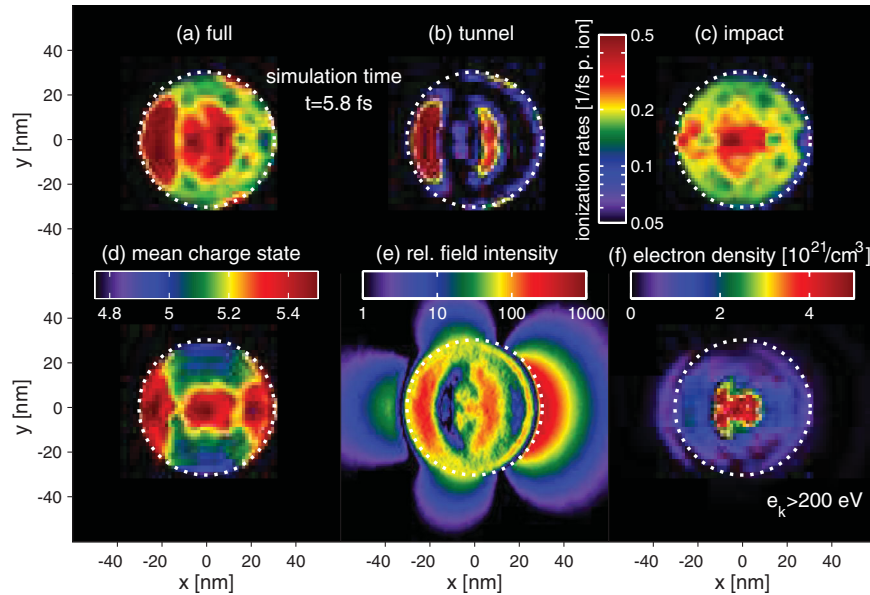


FIG. 3 (color). Detailed snapshot of the run in Fig. 2 at $t = 5.8$ fs. Shown are spatial distributions of total, tunnel, and impact ionization rates (a)–(c), mean Xe charge states (d), electric field intensity normalized to peak laser field intensity E^2/E_0^2 (e), and fast electrons (f) with kinetic energy $e_k > 200$ eV.

phase-space distribution and high local electric fields [Figs. 2(k) and 2(l)]. The resulting charge density and field fluctuations take place on a nanometer space and atto-second time scale.

Figure 3 shows the effect of the plasma-wave dynamics on the cluster ionization. The key signature is a pronounced spatial modulation of the tunnel and impact ionization rates; see Figs. 3(a)–3(c) for a time near the end of the laser pulse. First, regions with a high tunnel ionization rate can be clearly assigned to hot spots of the field intensity [Figs. 3(b) and 3(e)]. These hot spots are created by the propagation and collision of the plasma waves and exceed the laser peak intensity by more than 2 orders of magnitude. Second, impact ionization depends mainly on the electrons kinetic energy, which is determined by the plasmon collective motion on which the plasma-wave dynamics is superimposed. Hot spots with high densities of fast electrons are created where these two contributions are maximal and act in the same direction, resulting in enhanced impact ionization [Figs. 3(c) and 3(f)]. The correspondence between hot electrons and impact ionization is distorted by the fact that high electric fields suppress the ionization barrier and also enhance impact ionization. The enhanced ionization caused by the plasma-wave induced field and fast electron hot spots results in a pronounced nonuniform spatial charge state distribution in the cluster [Fig. 3(d)]. Ionization increases the resonance frequency by about 10% over the laser pulse and creates charges up to Xe^{10+} in the cluster.

The observed plasma-wave dynamics and the resulting nonuniform, enhanced ionization are of particular interest for understanding laser-excited clusters and microdroplets

[24], which are a promising medium for the development of highly charged ion [25] and x-ray [26] sources. Moreover, the plasma-wave induced field enhancement takes place in the nonlinear, nonperturbative laser-matter interaction realm, which adds a new facet to the hot topic of nanoplasmonics that has so far been studied in the linear response regime [27].

Furthermore, the regular wave to turbulent dynamics transition is of fundamental interest for fluid dynamics and plasma physics. MicPIC enables a rigorous analysis of turbulence with microscopic or atomic resolution, which is not feasible with existing methods. Combined with ultrafast x-ray imaging [28], we expect new insights in the making and breaking of waves in finite plasmas.

Finally, MicPIC holds the potential to explore so far inaccessible regimes of laser-matter interaction, such as a microscopic analysis of laser machining and the modification of solids and droplets with infrared to extreme ultraviolet radiation [28–31].

Financial support from the Deutsche Forschungsgemeinschaft within SFB 652/2 and computer time at the HLRN and CLUMEQ Computing Centers are gratefully acknowledged.

*cvarin@uottawa.ca

†thomas.fennel@uni-rostock.de

- [1] S. Pfalzner and P. Gibbon, *Phys. Rev. E* **57**, 4698 (1998).
- [2] J. M. Dawson, *Rev. Mod. Phys.* **55**, 403 (1983).
- [3] C. K. Birdsall and A. B. Langdon, *Plasma Physics Via Computer Simulation* (McGraw-Hill, New York, 1985).

- [4] J.P. Verboncoeur, *Plasma Phys. Controlled Fusion* **47**, A231 (2005).
- [5] J. Barnes and P. Hut, *Nature (London)* **324**, 446 (1986).
- [6] S. Pfalzner and P. Gibbon, *Many-Body Tree Methods in Physics* (Cambridge University Press, Cambridge, 1996).
- [7] J. Eastwood and R. Hockney, *J. Comput. Phys.* **16**, 342 (1974).
- [8] U. Saalmann, C. Siedschlag, and J.M. Rost, *J. Phys. B* **39**, R39 (2006).
- [9] Th. Fennel, K.-H. Meiwes-Broer, J. Tiggesbäumker, P.-G. Reinhard, P.M. Dinh, and E. Suraud, *Rev. Mod. Phys.* **82**, 1793 (2010).
- [10] A. Pukhov and J. Meyer-ter-Vehn, *Phys. Rev. Lett.* **76**, 3975 (1996).
- [11] T.V. Liseykina, S. Pirner, and D. Bauer, *Phys. Rev. Lett.* **104**, 095002 (2010).
- [12] A. Pukhov, *Rep. Prog. Phys.* **66**, 47 (2003).
- [13] T. Takizuka and H. Abe, *J. Comput. Phys.* **25**, 205 (1977).
- [14] T. Nakamura, Y. Fukuda, and Y. Kishimoto, *Phys. Rev. A* **80**, 053202 (2009).
- [15] M. Nantel, G. Ma, S. Gu, C. Y. Côté, J. Itatani, and D. Umstadter, *Phys. Rev. Lett.* **80**, 4442 (1998).
- [16] L. Ramunno, Ch. Jungreuthmayer, H. Reinholz, and T. Brabec, *J. Phys. B* **39**, 4923 (2006).
- [17] C. Siedschlag and J.M. Rost, *Phys. Rev. Lett.* **89**, 173401 (2002).
- [18] T. Fennel, L. Ramunno, and T. Brabec, *Phys. Rev. Lett.* **99**, 233401 (2007).
- [19] C. Jungreuthmayer, M. Geissler, J. Zanghellini, and T. Brabec, *Phys. Rev. Lett.* **92**, 133401 (2004).
- [20] See Supplemental Material at <http://link.aps.org/supplemental/10.1103/PhysRevLett.108.175007> for further technical details on methodology.
- [21] A. Taflove and S.C. Hagness, *Computational Electrodynamics: The Finite-Difference Time-Domain Method* (Artech House, Norwood, MA, 2005).
- [22] J.A. Stratton, *Electromagnetic Theory* (Wiley-IEEE Press, Hoboken, NJ, 2007).
- [23] T. Ditmire, T. Donnelly, A.M. Rubenchik, R.W. Falcone, and M.D. Perry, *Phys. Rev. A* **53**, 3379 (1996).
- [24] R. Thiele *et al.*, *Phys. Rev. E* **82**, 056404 (2010).
- [25] T. Ditmire, J.W.G. Tisch, E. Springate, M.B. Mason, N. Hay, R.A. Smith, J. Marangos, and M.H.R. Hutchinson, *Nature (London)* **386**, 54 (1997).
- [26] F. Dorchies, F. Blasco, C. Bonté, T. Caillaud, C. Fourment, and O. Peyrusse, *Phys. Rev. Lett.* **100**, 205002 (2008).
- [27] M. Stockman, *Phys. Rev. Lett.* **93**, 137404 (2004).
- [28] H.N. Chapman *et al.*, *Nature Phys.* **2**, 839 (2006).
- [29] L. Englert, M. Wollenhaupt, L. Haag, C. Sarpe-Tudoran, B. Rethfeld, and T. Baumert, *Appl. Phys.* **92**, 749 (2008).
- [30] V.R. Bhardwaj, E. Simova, P.P. Rajeev, C. Hnatovsky, R.S. Taylor, D.M. Rayner, and P.B. Corkum, *Phys. Rev. Lett.* **96**, 057404 (2006).
- [31] C. Bostedt *et al.*, *Phys. Rev. Lett.* **100**, 133401 (2008).